Applied Catalysis B: Environmental 181 (2016) 445–455

Contents lists available at ScienceDirect

Applied Catalysis B: Environmental

journal homepage: www.elsevier.com/locate/apcatb

Rh-decorated $PtIrO_x$ nanoparticles for glycerol electrooxidation: Searching for a stable and active catalyst

Cinthia R. Zanata[a,b], Pablo S. Fernández[c], Horacio E. Troiani[d], Analía L. Soldati[d], Richard Landers[e], Giuseppe A. Camara[b], Adriana E. Carvalho[a], Cauê A. Martins[a,*]

[a] Faculty of Exact Sciences and Technology, Universidade Federal da Grande Dourados, 79804-970 Dourados, MS, Brazil
[b] Institute of Chemistry, Universidade Federal de Mato Grosso do Sul, C.P. 549, 79070-900 Campo Grande, MS, Brazil
[c] Institute of Chemistry, Universidade Estadual de Campinas. Cidade Universitária "Zeferino Vaz", Barão Geraldo, CEP 13083-970 Campinas, SP, Brazil
[d] División Fisica de Metales, Centro Atómico Bariloche, Av. Ezequiel Bustillo 9500, San Carlos de Bariloche (8400) RN, Argentina
[e] Department of Applied Physics, Instituto de Física Gleb Wataghin, Universidade Estadual de Campinas, 13083-859, Campinas, SP, Brazil

ARTICLE INFO

Article history:
Received 20 April 2015
Received in revised form 3 July 2015
Accepted 10 August 2015
Available online 12 August 2015

Keywords:
Fuel cells
Iridium oxides
Rhodium
Glycerol electrooxidation
Stability

ABSTRACT

We report a fast method of producing rhodium-decorated platinum nanoparticles (NPs) containing iridium oxides (IrO_x) to be used in the glycerol electrooxidation reaction. We synthesize $PtIrO_x$/C electrocatalysts of different atomic compositions dispersed on Carbon Vulcan XC-72R® by using the fast polyol method assisted by microwaves. Afterwards, $PtIrO_x$/C was potentiodynamically decorated by Rh (Rh/$PtIrO_x$/C). The NPs are characterized by energy dispersive X-ray analysis, X-ray diffraction, X-ray photoelectron spectroscopy and transmission electron microscopy. The electrooxidation of glycerol was investigated in acid medium by cyclic voltammetry and chronoamperometry. The electrochemical stability of Rh/$PtIrO_x$/C NPs was evaluated by following a degradation test protocol, which consists in exhaustive cyclic voltammetries. Our results show that the presence of iridium oxides in the architecture of platinum enhances the electrochemical stability of the catalyst by avoiding agglomeration effects. Moreover, the presence of rhodium catalyzes the glycerol electrooxidation reaction. These results help understanding the role of Rh and IrO_x in the glycerol electrooxidation and provide new insights for designing nanomaterials with improved stability and activity.

© 2015 Elsevier B.V. All rights reserved.

1. Introduction

Fossil fuels are finite and environmentally aggressive, which leads to an intensive searching for alternative energy sources. Fuel cells fed by H_2 produce energy with low environmental impact, since they generate power from two coupled chemical reactions – oxidation of H_2 and reduction of O_2 – to produce water. Direct alcohol fuel cells (DAFC), fed by methanol and ethanol for example, present some advantages compared to H_2, namely: High volumetric and gravimetric energy densities, high energy efficiencies, easier storage and transportation [1].

Glycerol has emerged as a potential fuel to feed anodes of direct alcohol fuel cells [2] due to its high theoretical energy (14 electrons per molecule, considering its total conversion to CO_2) and availability, since it is a massive co-product of biodiesel fabrication. It is well-known that both the low ability of Pt nanoparticles (NPs) in cleaving C—C bonds of alcohols and its low CO tolerance diminish the output efficiency of the systems based on these materials [2–6]. Specifically regarding the glycerol electrooxidation reaction (GEOR), despite the relative little knowledge about its mechanism of oxidation, some important aspects have been unfolded in recent years. For instance, we know that important amounts of CO_2 can be obtained during the GEOR on Pt surface in acid media [7] and results of *in situ* FTIR applied to isotopically-labeled glycerol suggested that a full glycerol oxidation can be achieved under certain experimental conditions [8]. However, in a later study, our research group reported that CO_2 is mainly produced through a sequential pathway, with each step involving few electrons [9]. Thus, although the production of CO_2 indicates C—C splitting, it is not a guarantee of high energetic content. Therefore, further studies correlating the electrochemical current and the substances produced during the GEOR are still required.

Many efforts have been made to identify the products and intermediates of the GEOR. Recent papers showed that glycerol yields a myriad of products and intermediates from its electrooxidation on Pt surfaces. By comparing *in situ* FTIR spectra collected during

* Corresponding author. Fax: +55 34102089.
E-mail address: cauemartins@ufgd.edu.br (C.A. Martins).

http://dx.doi.org/10.1016/j.apcatb.2015.08.021
0926-3373/© 2015 Elsevier B.V. All rights reserved.

the GEOR in acid solution with standard FTIR spectra of several carbonyl compounds, Gomes and Tremiliosi-Filho suggested that tartronic acid, glycolic acid, glyoxylic acid, formic acid and CO_2 are produced during the GEOR [10]. Under the operational potential of fuel cells, glycerol shall produce mainly glyceraldehyde and glyceric acid [11,12]. Thereby, its reaction demands new materials to accelerate the oxidation of partially oxidized species.

The identification of stable materials that can electro-catalyze glycerol toward the high efficient pathway remains a key obstacle to the commercialization of the direct glycerol fuel cells. To overcome these difficulties, many efforts have been made concerning the development of catalysts. Kwon et al. reported a 100% selectivity of glycerol electrooxidation towards dihydroxyacetone on bismuth modified Pt/C NPs [13]. This outstanding selectivity evidences the possibility of guiding the pathways of this complex reaction. By using online HPLC experiments, these authors showed that Pt/C catalyst mainly produces glyceraldehyde and glyceric acid at low potentials and formic acid at high potentials in acid solution [12,13].

At least under our concern, there is no work regarding the use of PtRh NPs assisted by oxide metals (MO_x) for GEOR in acid media. But similar materials have been used to electrooxidize other biomass-derived alcohols. It has been reported that the cleavage of C-C bonds in alcohols is enhanced if rhodium is alloyed with Pt and assisted by a metallic oxide in acid media [14–16] or alloyed with Pd in alkaline media [17]. Following the works of Kowal et al., regarding the role of $PtRhSnO_2/C$ surfaces on the ethanol electrooxidation reaction (EEOR) [18,19], Silva et al. reported that NPs containing more than 10% of Rh in PtRh/C NPs hinder the EEOR, although that accurate composition seems to improve the reaction. Furthermore, the ternary PtRhSn/C (containing SnO_2 species) seems to enhance the adsorption and oxidation of ethanol. The authors also argue that SnO_2 seems not to drive the reaction toward the complete oxidation; however, the ternary catalyst showed the maximum production of CO_2 among the electrodes studied [16]. Although there is no concrete and clear evidence of the role of Rh and MO_x on the alcohol electrooxidation, it is accepted that rhodium promotes C-C cleavage while the metal-oxide seems to provide O species for the electrooxidation of intermediates during the reaction on Pt surface [15,20]. Therefore, platinum–rhodium assisted by metal-oxide NPs seems to have their own role at the fuel cells scenario.

Apart from promoting a fast reactants-products conversion and the ability of splitting C-C bonds, the catalytic surface must be electrochemically stable [21]. There are few works dealing with stability of nanocatalysts for glycerol electrooxidation. On the other hand, there are plenty of papers regarding the electrochemical stability of nanomaterials to be used as cathode. In both instances, anode and cathode, the catalysts are submitted to several consecutive cyclic voltammetries and the surface area is followed as criterion of stability. Therefore, works reporting the stability of materials for oxygen reduction or evolution at the cathode can be usually extrapolated for the anode. In this context, IrO_2 and RuO_2 have emerged as alternatives to classic catalysts [22,23]. Reier et al. evaluated the stability of Pt, Ru and Ir on bulk and nanoscaled surfaces. They found that in spite of the outstanding activity of Ru for oxygen evolution reaction, this metal (used alone) does not meet the stability required for fuel cells application. On the other hand, Ir seems to carry high stability and acceptable activity [24]. Wesselmark et al. deposited Pt and Ir in a gas diffusion layer for long-term tests in fuel cells [23] and the stability of the electrodes containing Ir was improved compared to sole Pt.

In addition to the high stability, some works showed a relevant contribution of Ir (and the metal-oxide form, IrO_2) on the improvement of the electroactivity of Pt-based catalysts. Ribeiro et al. showed that PtSnIr/C improved the ethanol electrooxidation compared to PtIr and Pt/C [25]. Ehab et al. studied co-electrodeposited PtIr on Au, finding Pt_3Ir_1 as the optimum surface for methanol electrooxidation reaction in sulfuric acid solution [26]. Therefore, it is plausible that Ir can contribute to the fabrication of an electrochemically stable and multifunctional surface, which can modify the glycerol electrooxidation pathway towards a higher efficient catalyst.

Kowal et al. have studied a complex multimetallic catalyst composed by Pt, Ir and Rh in the presence of SnO_2 toward EEOR. In a pioneer investigation, they showed that $PtIrRh/SnO_2/C$ nanoparticle catalyst intensely shifts the onset potential of ethanol oxidation towards more negative potentials while promotes the formation of CO_2 in acid solution [18].

As far as we are concerned, there are no studies about the influence of Ir on GEOR. Furthermore, systematic studies focusing on the effect of multimetallic nanoscalling catalysts containing metal-oxides in their structure for glycerol electrooxidation are missing to date. In this context, based on the previous reports regarding the electrooxidation of small chain biomass-derived alcohols, we present an investigation of the GEOR on nanoscaled $PtIrO_x/C$ and Rh-decorated $PtIrO_x/C$ electrocatalysts to reveal trends in their catalytic performance and electrochemical stability.

2. Experimental

2.1. Synthesis of carbon supported metallic nanoparticles

Solutions for synthesis were prepared using ethylene glycol (J. T. Baker), poli(acrylic acid sodium salt) (impurities < 15% water; pH 6.0-9.0, 10 mg/mL in water; cation traces, Na ~ 19%; Sigma–Aldrich), H_2PtCl_6, $IrCl_3$, $RhCl_3$ (Sigma–Aldrich) and 2-propanol (Vetec).

Pt/C, IrO_x/C and $Pt_{1-w}(IrO_x)_w/C$ NPs were synthesized for the first time by using the fast polyol method assisted by microwaves [27] with slight modifications. Briefly, adequate amounts of H_2PtCl_6, $IrCl_3$, poly(acrylic acid sodium salt) (PA) and 20 mL of solution 3:1 of ethylene glycol (EG): water were mixed in ultrasonic bath during 5 min followed by the addition of Carbon Vulcan XC72® and sonication for additional 20 min. The nominal Pt:Ir atomic ratios were set to 100:0, 75:25, 50:50, 27:75 and 0:100. The PA/metal ratio was adjusted to 5.0 in an attempt to obtain well dispersed NPs [27] and the metal load was set to 40%. The dispersion was heated during 30 s using a household microwave oven. The dispersions containing the nanoparticles were washed with deionized water and centrifuged 5 times to eliminate synthesis residues and finally dried in oven under 60 °C during 24 h, resulting in a black powder. The Rh-decorated electrode will be described in due course through the text.

2.2. Preparation of carbon supported electrodes and electrochemical measurements

The dispersions of NPs (inks) were prepared by adding 1 mg of the nanoparticle powder in a vial with 50 μL of Nafion® (Aldrich 5% v/v) and 2 mL of water. Afterwards, each dispersion was sonicated for 20 min and an aliquot of 150 μL of the corresponding ink was immobilized on a 0.98 cm^2 Au disk (polished to a mirror finish and kept at 50 ± 2 °C), followed by the dropping of 50 μL of a diluted Nafion® solution (1 mL of Nafion® 5%:20 mL of 2-propanol). This protocol was repeated for all samples and the corresponding dispersions were used as working electrodes. Prior to the preparation of the catalysts, the Au disk was meticulously cleaned with acetone, 2-propanol and water in ultrasonic bath, followed by an electrochemical cleaning between 0.05 and 1.75 V (*vs.* RHE). Afterwards, the Au profile was recorded to guarantee the reliability of

the measurements. Fig. S1 shows a representative profile of the Au disk (in meniscus configuration).

The electrochemical experiments were carried out using a conventional oxygen-free (N_2 saturated solution) three-electrode cell in 0.1 mol L^{-1} $HClO_4$ connected to a Potentiostat/Galvanostat μAutolab. The NPs deposited on Au were used as a working electrode, a high surface area Pt electrode was used as counter electrode and a reversible hydrogen electrode (RHE) as reference. All electrochemical runs were performed at 25 °C. The electrochemical characterization of the catalysts in 0.1 mol L^{-1} $HClO_4$ was obtained in the potential range of 0.05–1.45 V at 0.05 V s^{-1}. The electrochemical response of the catalysts in presence of glycerol was evaluated in 0.1 mol L^{-1} $HClO_4$ + 0.2 mol L^{-1} glycerol solutions at 0.05 V s^{-1}, using the following potential protocol: 0.05 V → 1.45 V for $PtIrO_x$/C and 0.05 V → 1.35 V for Rh-decorated $PtIrO_x$/C NPs, both starting at 0.12 V. The potential of 0.12 V was used to minimize undesirable reactions during the standby potential, as the reduction of glycerol to propane [28]. The upper potential was set to 1.35 V for the Rh-decorated electrodes, according to previous works [16]. The current densities (j) were calculated from the ratio between the measured current and the electrochemically active surface area (ECSA) of Pt, calculated by considering 210 μC as the charge involved in the desorption of one monolayer of hydrogen per square centimeter.

2.3. Cleaning and surface conditioning of the catalysts

The microwaves-assisted EG method of synthesizing NPs is simple, fast and produces well-dispersed NPs. However, some residues are usually found on the metal surfaces, as partially oxidized ethylene glycol and leavings of the stabilizing agent [29]. In this sense, we have applied an electrochemical cleaning protocol to remove such residues and maximize the use of the catalyst surface [27,30]. In this method, the working electrode is cycled multiple times, usually between the formation and reduction of surface oxides. In this work, the cleaning protocol has an additional role of producing stable IrO_x. Thus, here we performed 100 cycles between 0.05 and 1.45 V as a way to cleaning and conditioning the electrode surface at the same time. As widely spread in literature, this process induces some agglomeration [21]. In this sense, we monitored the ECSA of Pt/C synthesized by the present method *vs.* the number of potential cycles imposed to the catalysts. The ECSA depicts an initial increase up to the 10th cycle followed by a slight decrease, as shows Fig. S2. Such behavior can be rationalized as being due the surface cleaning process (which increases the ECSA) followed by some agglomeration in the subsequent cycles (responsible for the converse effect) [31]. Approximately 10 cycles seems to be enough for a reasonable cleaning of the surface with minimum agglomeration, but they are not sufficient for producing stable IrO_x surface (as discussed later). Therefore, we have chosen 100 cycles as cleaning-conditioning protocol, which in turn leads to a loss of ~14% of the initial area. This protocol was followed for all catalysts.

2.4. Physical characterization of the materials

The as-prepared NPs were characterized by transmission electron microscopy (TEM) and high resolution TEM (HRTEM), recorded in a CM 200 Philips equipment, which operates with a LaB_6 emission gun. The microscope is equipped with an ultratwin objective lens and it was operated at 200 keV. The mean diameter of NPs was determined by using the software Axio Vision SE64 Rel.4.8.

The crystallographic structure of the NPs was investigated by X-ray diffraction (XRD), recorded in a Siemens model D5000 powder diffractometer, equipped with a monochromatic Cu Kα X-ray source. Diffraction data were collected by step scanning with a step size of 0.02° between 5° and 90°.

The chemical composition of the catalysts was determined by using an Energy Dispersive X-ray (EDX) detector coupled to a scanning electron microcopy JEOL model JSM6380-LV. The EDX experiments were performed in triplicate.

The XPS spectra were measured with a VSW HA100 electron analyzer in the fixed analyzer transmission mode (FAT) with a pass energy of 44 eV. Al Kα radiation was used for excitation (1486.6 eV). The vacuum in the analysis chamber was in the low 10^{-8} mBar range. The analyzer was calibrated using the Au $4f_{7/2}$ line at 84 eV. To minimize a possible influence of the carbon support the powder samples were pressed on to a freshly cut Indium surface and immediately introduced into the vacuum. For each sample a survey scan and detailed scans of the regions of interest were collected. A Shirley type background [32] was subtracted and due to the overlap of the Pt 4f X-ray satellites (α3,4) with the Ir 4f line we also subtracted the satellites from the spectra prior to the fitting procedure. For the fitting we used Gaussian line shapes and imposed constraints so that parameters such as multiplet splitting and the statistical ratios between the multiplet components were respected. To determine the composition, Scofield [33] cross sections were used and the intensities corrected for analyzer transmission and the mean free paths associated with the different kinetic energies of the photoelectrons. Lastly the composition was considered as homogeneous throughout the sampled region.

3. Results and discussion

3.1. Physical characterization

The real atomic composition of the NPs determined by EDX and the respective standard deviations are summarized in Table S1. The compositions obtained by EDX are different from the respective nominal ones. The moderate reducing agent and the short time of synthesis could be a reason for such discrepancy. Nevertheless, this easy and fast procedure allows us obtaining nanomaterials of several compositions, providing the first insights concerning the influence of IrO_x on the GEOR. From now on, the catalysts will be named according to their real composition as follows: Pt/C, $Pt_{95}(IrO_x)_5$/C, $Pt_{83}(IrO_x)_{17}$/C, $Pt_{70}(IrO_x)_{30}$/C and IrO_x/C.

To estimate the composition of the catalysts for other independent and different method than EDX and to gain some insight about the oxidation states of Pt and Ir, we performed XPS measurements. Pt and Ir 4f states were measured and fitted. Table S2 shows the binding energies, relative areas of the fitted peaks and the calculated atomic composition for each catalyst. XPS measurements revealed an atomic composition close to that determined by EDX. All Pt signals were fitted by two peaks, corresponding to Pt(0) and Pt oxides, located at ~71.5 and 74.0 eV, respectively. For all catalysts, most of the Pt is in metallic state. $Pt_{70}(IrO_x)_{30}$ has the higher content of Pt oxides (35%).

To identify the phase of Ir in the nanostructure, their signals were fitted with one or two peaks with binding energies between 60.7–61.0 eV for Ir(0) and 62.0–62.4 eV for Ir oxides. Ir is in the metallic state for the material containing the lower Ir amount, but we keep the label $Pt_{95}(IrO_x)_5$/C for convenience because the catalyst used is the $Pt_{95}Ir_5$/C conditioned to form IrO_x. Conversely, the Ir/C catalyst is totally composed of Ir oxides. For $Pt_{83}(IrO_x)_{17}$/C and $Pt_{70}(IrO_x)_{30}$/C the percentages of metallic Ir are ~72% and 59%, respectively.

XPS measurements also provide the metal/carbon ratio w/w. The amount of metals relative to carbon decreases as the synthesis solution is enriched by Ir, namely: 26% for Pt/C, 26% for $Pt_{95}(IrO_x)_5$/C, 24% for $Pt_{83}(IrO_x)_{17}$/C, 17% for $Pt_{70}(IrO_x)_{30}$/C and 2% for IrO_x/C. This result is reasonable because Ir is less likely to be reduced than Pt. Thus, IrO_x/C was the catalyst most affected for

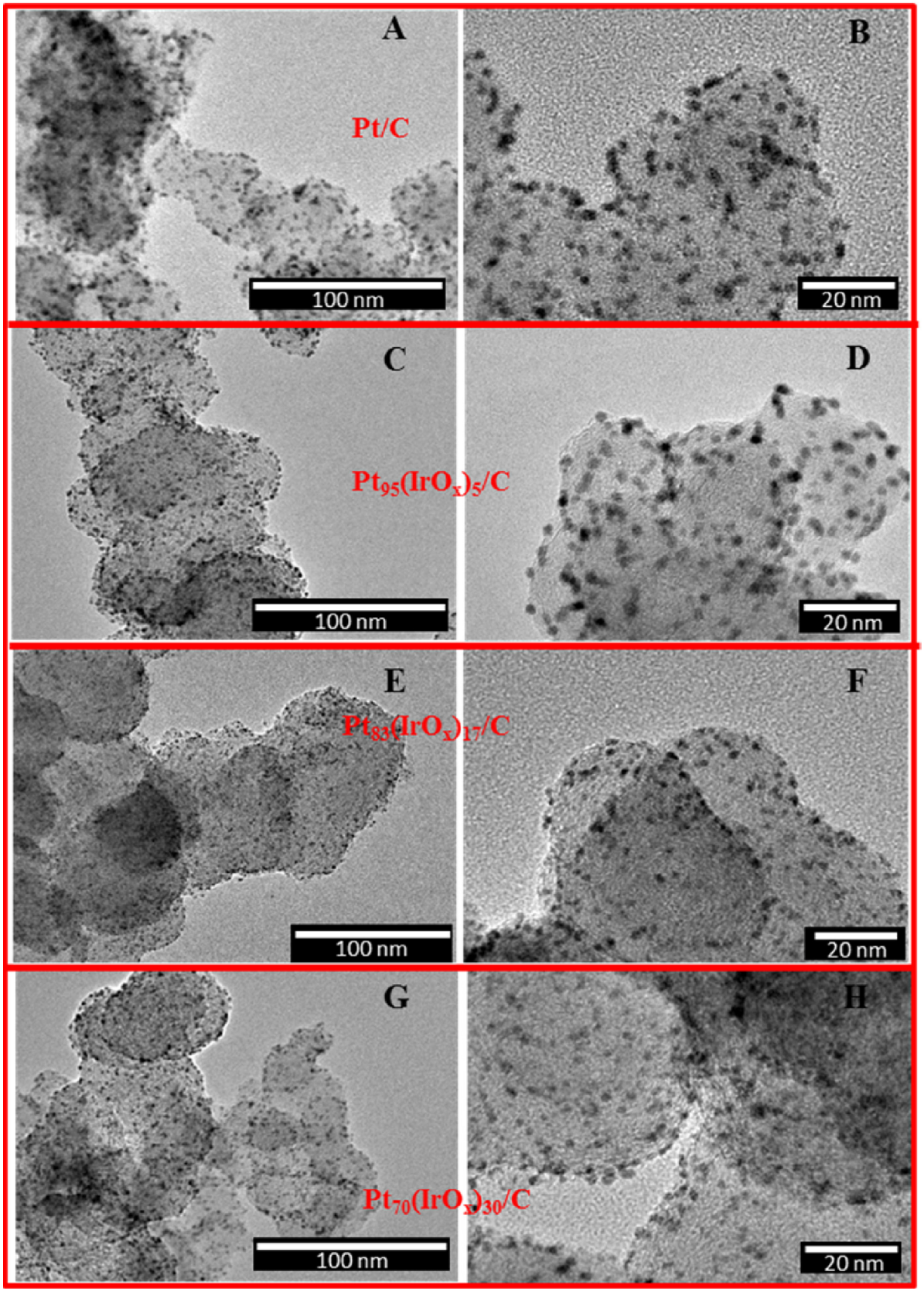

Fig. 1. TEM micrographs of Pt/C (A and B), $Pt_{95}(IrO_x)_5/C$ (C and D), $Pt_{83}(IrO_x)_{17}/C$ (E and F) and $Pt_{70}(IrO_x)_{30}/C$ (G and H).

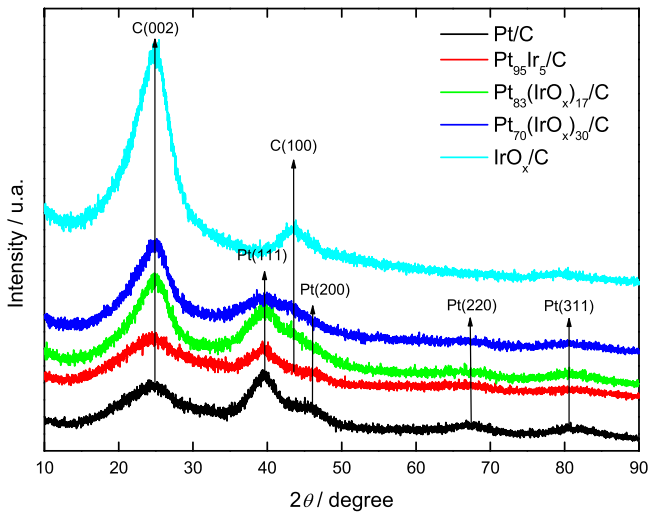

Fig. 2. XRD patterns of Pt/C (black curve), $Pt_{95}(IrO_x)_5/C$ (red curve), $Pt_{83}(IrO_x)_{17}/C$ (green curve), $Pt_{70}(IrO_x)_{30}/C$ (blue curve) and IrO_x/C (cyan curve). (For interpretation of the references to colour in this figure legend, the reader is referred to the web version of this article.)

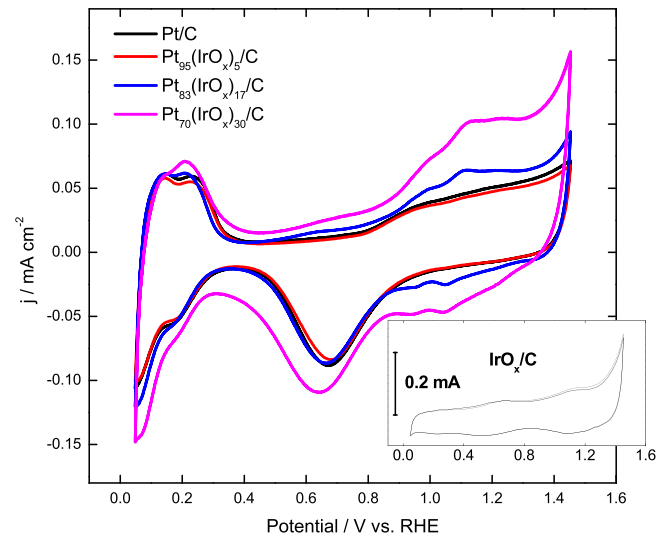

Fig. 3. The electrochemical behavior of Pt/C (black), $Pt_{95}(IrO_x)_5/C$ (red), $Pt_{83}(IrO_x)_{17}/C$ (blue), $Pt_{70}(IrO_x)_{30}/C$ (magenta) and IrO_x/C (inset) in 0.1 mol L^{-1} $HClO_4$ between 0.05 and 1.45 V at 0.05 V s^{-1}.(For interpretation of the references to colour in this figure legend, the reader is referred to the web version of this article.)

the mild reducing conditions, presenting only 2% w/w of IrO_x. The metal loading of Pt/C and $Pt_{95}(IrO_x)_5/C$ is close, which allows us to compare the activity of these catalysts in terms of their chemical compositions.

The morphology, the distribution of NPs over the support and the size distribution of the catalysts are shown in Fig. 1. The Pt NPs synthesized by microwave-assisted polyol method are remarkably well distributed over the carbon support and extremely small, in agreement of some reports concerning chemical reducing methods [34–36]. Pt (Fig. 1A–B) and $Pt_{1-w}(IrO_x)_w/C$ (Fig. 1C–H) NPs do not have defined and uniform morphology, although they are mostly spherical. The NPs present a few regions of agglomeration, mainly observed for Pt/C (Fig. 1A).

The mean diameter of the NPs was investigated by counting at least 200 particles of a set of high resolution micrographs for each catalyst. The average sizes were 2.4 ± 0.5 nm for Pt/C; 2.3 ± 0.4 nm for $Pt_{95}(IrO_x)_5/C$; 2.2 ± 0.3 nm for $Pt_{83}(IrO_x)_{17}/C$; and 2.2 ± 0.5 nm for $Pt_{70}(IrO_x)_{30}/C$. All catalysts showed similar size and morphology. Although EDX and XPS results provide concrete evidences of the presence of IrO_x in IrO_x/C material, TEM and HRTEM of the IrO_x/C sample have not presented any clear definition of NPs. Hence, we were not able to estimate the mean diameter of the non Pt-based nanomaterial from the micrographs. The difficulty in finding the IrO_x/C is probably due to the extremely low content of metal oxide on carbon (2%, as shows Table S2).

Fig. 2 shows that all X-ray diffraction patterns corresponding to the as-prepared nanomaterials exhibit the (002) reflection peak of the carbon structure of Vulcan XC72® [37,38]. The XRD patterns also present broad peaks in all cases, which can be due to the very small size of the particles [34–36]. Despite the low definition of the peaks, we can clearly identify the (1 1 1), (2 0 0), (2 2 0) and (3 1 1) reflection peaks of Pt [39], as shows the black curve in Fig. 2.

The peaks related to Ir are probably hidden behind the broad peaks of Pt, which is in agreement with the literature [40]. Besides, the low content of IrO_x prevents the diffraction peaks to be discernible in Fig. 2. However, a peak at 2θ ~43.6 increases as the metal loading decreases and it is obvious for IrO_x/C. This peak is ascribed to a (1 0 0) reflection of the carbon structure [41].

3.2. The electrochemical characterization of $PtIrO_x/C$ catalysts

Fig. 3 shows the voltammetric profiles of the catalysts after cleaning and conditioning the surface. The synthesized Pt/C shows the ordinary electrochemical behavior in 0.1 mol L^{-1} $HClO_4$, with hydrogen underpotential deposition (UPD) region between 0.05 and 0.32 V, the formation of Pt-oxides (starting at ~0.80 V) and the reduction of Pt-oxides centered at ~0.67 V. The addition of few amounts of IrO_x in the structure slightly affects the hydrogen UPD region, as show red and blue curves of Fig. 3, for 5 and 17 % of IrO_x on the catalyst, respectively. The presence of 5 and 17% of IrO_x sorely changes the Pt-oxide region of the electrodes. The onset potential for the formation of surface oxides is a little delayed, but a new couple of formation/reduction of oxides arises at ~1.12 and 1.04 V, which is more obvious for $Pt_{70}(IrO_x)_{30}/C$, as shows magenta curve in Fig. 3. Furthermore, the capacitive current region turns broader with the presence of irreversible oxides.

Moreover, as a global trend, the presence of IrO_x on the Pt structure displaces the metal oxide reduction peak towards more negative potentials, reaching 0.64 V for $Pt_{70}(IrO_x)_{30}/C$.

The electrochemical response of IrO_x is presented in the inset of Fig. 3, which shows the absence of hydrogen UPD region and the redox couples in the corresponding CV. These features are absent in the Pt/C profile but can be clearly noted in the materials containing Ir. Fig. S3 illustrates the manufacturing of such a surface by cycling the electrodes between 0.05 and 1.45 V, as previously reported by Podlovchenko et al. [42]. The surface conditioning protocol guarantees the presence of irreversible surface oxides, providing reproducibility among the experiments. Hence, we can infer from Figs. 3 and S3 that after surface conditioning $Pt_{95}(IrO_x)_5/C$ presents iridium in the oxidized form, although it was previously in metallic phase [42]. The decay of the currents in the hydrogen UPD region and an increase of two non-obvious sets of redox peaks indicate passivation [43]. The redox peaks at ~0.7 V and 1.2 V are ascribed to the Ir(III)/(IV) oxide and Ir(IV)/(V,VI) redox processes, respectively [44]. After successive cycles, part of the IrO_2 produced is not reduced to its metallic state and remains as IrO_x. A possible implication of the changes illustrated in Fig. S3 is that the Ir(IV) oxide layer generated in electrochemical environment is known to exhibit some porous structure [45], which might provide access to the adjacent metallic nanoparticles and modify the electrochemical response.

It is well-known that perchlorate ions in $HClO_4$ solution are subject to reductive attacks at a wide variety of electrodes. A special attention has been spent concerning Ir as a catalyst in the presence

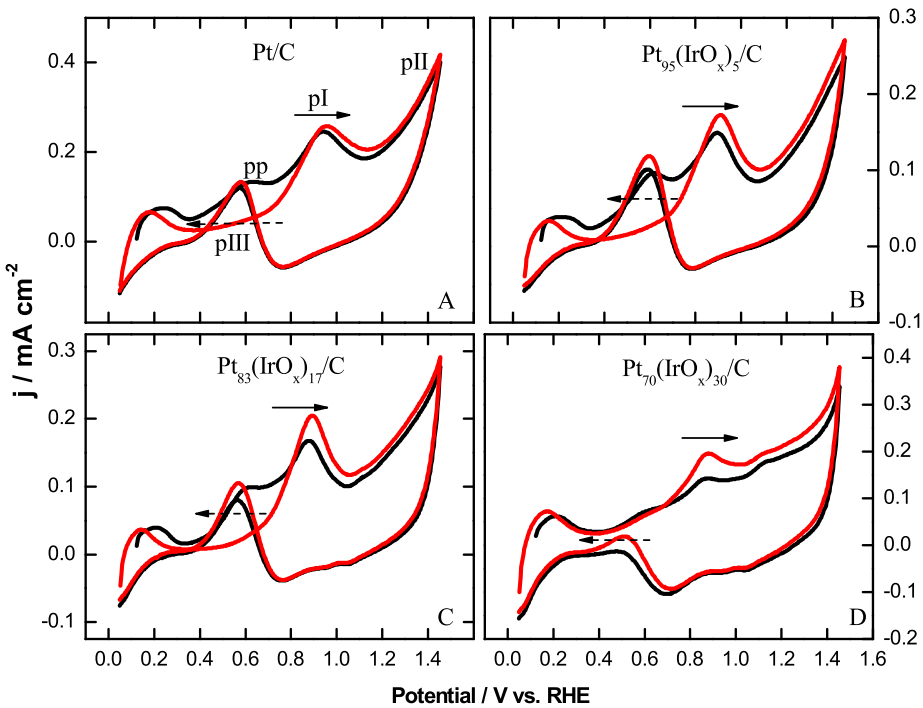

Fig. 4. The 1st (black curve) and 2nd (red curve) cyclic voltammograms of A. Pt/C, B. $Pt_{95}(IrO_x)_5/C$, C. $Pt_{83}(IrO_x)_{17}/C$, D. $Pt_{70}(IrO_x)_{30}/C$ nanoparticles in 0.1 mol L^{-1} $HClO_4$ + 0.2 mol L^{-1} glycerol between 0.05 and 1.45 V at 0.05 V s^{-1}. (For interpretation of the references to colour in this figure legend, the reader is referred to the web version of this article.)

of perchlorate ions [46,47]. To avoid contamination of Ir electrodes by chloride, Reier et al. performed an electrochemical characterization in sulfuric acid media prior to evaluate the electroactivity of those catalysts [24]. Accordingly, we performed CVs of IrO_x/C electrode in 0.1 mol L^{-1} H_2SO_4 and the response was close to that observed in $HClO_4$, corroborating that in that case the NPs are already initially oxidized (Fig. S4). Furthermore, a possible presence of ClO_4^- in solution would influence all catalysts in the same way, then, it seems reasonable do not consider that variable for the present discussion.

Now, considering the aforementioned catalysts, we discuss the influence of IrO_x on the activity of Pt/C NPs toward GEOR.

3.3. The electrooxidation of glycerol on $PtIrO_x/C$ surfaces

Fig. 4A shows the voltammetric profile of GEOR on Pt/C in 0.1 mol-L^{-1} $HClO_4$. The detailed discussion regarding the electrooxidation of glycerol on bulk Pt polycrystalline [48], Pt single crystals [49] and Pt/C NPs [30] can be accessed in previous works.

Pt/C NPs present four discernible anodic peaks in the first cycle (black curve of Fig. 4A). During the positive potential going scan, there are three peaks: the first one is not well-defined and it is centered at ~0.6 V (hereafter denoted pp, from pre-peak), followed by a broad peak at ~0.9 V (pI), which leads to a subtle increase in the anodic current (pII). It has been reported that the pI is most likely comprised of two overlapping peaks, which are more obvious when the electrode is massive Pt [48], especially on those surfaces with orientation (1 1 1) [49], while the separation of signals is not well-defined for Pt NPs [30]. The currents decrease during the reverse sweep, reaching negligible values at 1.1 V. Finally, an abrupt reactivation of the surface is observed leading to an anodic peak centered at ~0.55 V (pIII). The potential range where glycerol oxidizes on Pt/C NPs showed here, can be rationalized as the outcome of a reaction taking place on non-organized surfaces, since the NPs are too small and do not present an uniform morphology.

The second cycle (red curve of Fig. 4A) differs from the first one mainly because the pp is absent. Similar behavior was previously reported by Fernández et al. [30]. Furthermore, the behavior of the first and second cycles of GEOR displays some other differences comparing the reaction on bulk and NPs. The pI seems to experience a potential delay in the second cycle on Pt bulk [48], while the delay observed for Pt/C NPs is less intense.

We recently demonstrated the relation between different Pt atomic structures and their potentiodynamic behavior towards GEOR [50]. Comparing our results with the previous one, we verify that Pt/C catalyst shows the main glycerol oxidation peak (pI) in the same potential domain that: (i) disordered Pt(1 1 0) and Pt(1 1 1) surfaces; (ii) Pt(1 0 0) ordered and disordered structures [50]. This result is reasonable since the NPs are very small and undefined shaped.

Overall, the current densities of the GEOR are higher on Pt/C than on $PtIrO_x/C$ catalysts (Fig. 4). No obvious features of glycerol oxidation were observed for IrO_x/C nanoparticles, indicating poor electroactivity. This result is consistent with the work of Chen et al., where the authors found no activity of Ir catalyst for formic acid oxidation in $HClO_4$ media [51]. However, the presence of IrO_x in the binary catalysts plainly changes the voltammetric features of glycerol oxidation. Both pp and pIII become better defined for $Pt_{95}(IrO_x)_5/C$ compared to Pt/C (see Fig. 4A and B). On the other hand, the current densities slightly decrease for $Pt_{83}(IrO_x)_{17}/C$ (Fig. 4C) and $Pt_{70}(IrOx)_{30}/C$ (Fig. 4D). This last catalyst also shows the lowest pI value among all (Fig. 4D), which suggests that high amounts of IrO_x are deleterious for the GEOR. In addition, $Pt_{95}(IrO_x)_5/C$ presents the highest pp/pI ratio, during the first cycle, which suggests that IrO_x plays an important role on the glycerol adsorption/oxidation steps. Furthermore, IrO_x apparently does not have the ability of shifting the onset potential of the pI towards more negative potentials (Figs. 4 and S5).

The first cycle is peculiar and the profile becomes virtually stable from the second cycle onwards [30]. In this sense, we compared the electrochemical parameters of the fifth cycle of the GEOR for all cat-

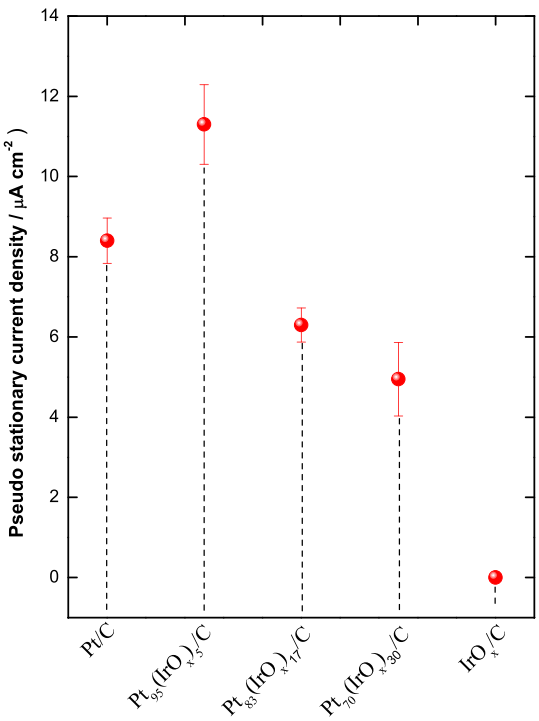

Fig. 5. Pseudo stationary current densities (referred to the active surface area) for glycerol oxidation, taken from current–time curves after 2100 s of polarization at 0.6 V (start potential of 0.12 V), plotted as a function of the composition of the catalysts.

alysts as shows Fig. S6 (the respective voltammograms are shown in Fig. S5). Firstly, the hydrogen UPD regions are different for the catalysts containing IrO_x and Pt/C (Fig. S5) after 5 oxidation cycles. The surfaces containing IrO_x remain covered with larger amounts of electrooxidation residues than Pt, resulting in a narrower hydrogen UPD region. Quantitatively, the current density of pI gentle differs among the catalysts. The largest contrast corresponds to 0.07 mA cm^{-2} between Pt/C and $Pt_{95}(IrO_x)_5$/C (Fig. S6), which is not a huge difference. The quotient between forward and backward anodic currents (jpI/jpIII in the present case) is usually used as criterion to evaluate the reactivation of a surface. The ratio jpI/jpIII is virtually the same for Pt/C, $Pt_{95}(IrO_x)_5$/C and $Pt_{83}(IrO_x)_{17}$/C, while it is sensibly higher for $Pt_{70}(IrO_x)_{30}$/C (Fig. S6). This result suggests that surfaces richer in IrO_x present a poorer ability of reactivation.

In order to estimate the influence of the composition on the glycerol electrooxidation in conditions closer to those experienced in fuel cells, we performed a series of chronoamperometric experiments. For such, the electrodes remained polarized at 0.12 V in solutions containing 0.1 mol L^{-1} $HClO_4$ + 0.2 mol L^{-1} glycerol. Afterwards, the potential was stepped to 0.6 V and hold for 2100 s (see representative chronoamperommetries in Fig. S7). The corresponding average of pseudostationary current densities for three experiments performed on each catalyst are showed in Fig. 5. The current density is negligible for IrO_x/C, while for $Pt_{95}(IrO_x)_5$/C it is fairly higher than for Pt/C. $Pt_{83}(IrO_x)_{17}$/C and $Pt_{70}(IrO_x)_{30}$/C presented lower current densities than Pt/C (Fig. 5), which corroborates the results taken from the potentio-dynamic experiments.

At this point, we decided to manufacture a new catalyst based on $Pt_{95}(IrO_x)_5$/C in an attempt to preserve its activity (observed in Figs. 4 and 5) and the high electrochemical stability of electrodes containing Ir [24]. Inspired by Vidal-Iglesias et al. [52], we used cyclic voltammetry to potentio-dynamically decorate $Pt_{95}(IrO_x)_5$/C surface with rhodium.

3.4. Electrochemically produced Rh-decorated Pt(IrO_x)/C catalyst

The $Pt_{95}(IrO_x)_5$/C electrode was conditioned as previously detailed. Afterwards, the catalyst was decorated with increasing amounts of Rh as follows: The Au disk containing a full layer of $Pt_{95}(IrO_x)_5$/C was placed in a meniscus configuration on a vessel containing a 2.2 mmol L^{-1} $RhCl_3$ + 0.1 mol L^{-1} $HClO_4$ solution; next, the electrode was transferred to an electrochemical cell containing 0.1 mol L^{-1} $HClO_4$ and submitted to 10 cycles between 0.05 and 1.35 V at 0.05 V s^{-1}, for each decoration step. The electrochemical decoration of $Pt_{95}(IrO_x)_5$/C with Rh is summarized in the scheme of Fig. 6A. We manufactured Rh-decorated $PtIrO_x$/C catalysts (hereafter named Rh/$Pt_{95}(IrO_x)_5$/C) by following one, two and three decoration steps (blue, black and magenta curves in Fig. 7A, respectively), and by cycling $Pt_{95}(IrO_x)_5$/C directly in an oxygen-free 2.2 mmol L^{-1} $RhCl_3$ + 0.1 mol L^{-1} $HClO_4$ solution (red curve in Fig. 7A). The micrographs of the Rh/$Pt_{95}(IrO_x)_5$/C NPs manufactured by following two decoration steps are shown in Fig. 6B–C. The NPs are remarkably well dispersed with a uniform morphology with 3.2 ± 0.6 nm as mean diameter. The Rh-decorated NPs presented an increase of size compared to the non-decorated $Pt_{95}(IrO_x)_5$/C (wich was 2.3 ± 0.4 nm). This enlargement could be rationalized as a contribution of two effects: (i) in a minor portion, the decoration step could lead to some agglomeration of the NPs [21,30]; (ii) the most important contribution is probably due to the growth of a rhodium layer of NPs on the $Pt_{95}(IrO_x)_5$ NPs. At this point is important to highlight that we discard the possibility of core-shell particle formation. Otherwise, we could not identify such a clear contribution of Pt in the electrochemical response.

Fig. 7A shows the effect of the progressive increase of Rh coverage on the surface of the $Pt_{95}(IrO_x)_5$/C nanoparticles. The increasing decoration can be correlated to the slight increase in the hydrogen desorption region and a deep increase of the hydrogen adsorption region. Moreover, a cathodic peak appears at ~0.4 V due to the presence of Rh, while the currents of the oxide formation region increase.

Fig. 7B shows the corresponding voltammetric profiles for glycerol electrooxidation. Results indicate a maximum electroactivity for the electrode manufactured by following two decoration steps (black curve in Fig. 7B) while the incorporation of greater amounts of Rh leads to a decrease of current, probably due to the blockage of active sites of Pt. The onset potential of glycerol electrooxidation (pI) is nearly the same for the whole series. On the other hand, the shape and current density of the anodic peaks change. pI and pII are more intense for the electrode decorated with two decoration steps. The catalyst with the lower coverage of Rh (blue curve) presents the highest surface reactivation while the surface richer in Rh shows the lowest surface reactivation. Interestingly, the electrodes submitted to one and three decoration steps and the completely covered one present the same current density in pI. Furthermore, covering of Rh with more than two decoration steps enlarges the anodic peak (magenta and red curves in Fig. 7B).

In an attempt to understand the morphology of the Rh-decorated NPs, we have performed the same protocol to potentio-dynamically electrodeposited Rh on carbon support. Fig. S8 shows the electrochemical profile of carbon support containing Rh in 0.1 mol L^{-1} $HClO_4$ in the absence and presence of 0.2 mol L^{-1} glycerol between 0.05 and 1.35 V at 0.05 V s^{-1}. The catalyst does not show clear characteristics of Rh deposition on carbon and does not exhibit any activity towards glycerol electrooxidation. Thereby, we can conclude that: (i) eventual amounts of Rh deposited on carbon during the electrochemical decoration of $Pt_{95}(IrO_x)_5$/C do not contribute to the activity of the nanomaterial; and (ii) the activity of Rh/$Pt_{95}(IrO_x)_5$/C NPs is due to the contribution of rhodium, iridium oxides and platinum gather together. This result suggests that most of Rh is deposited onto the $PtIrO_x$ particles.

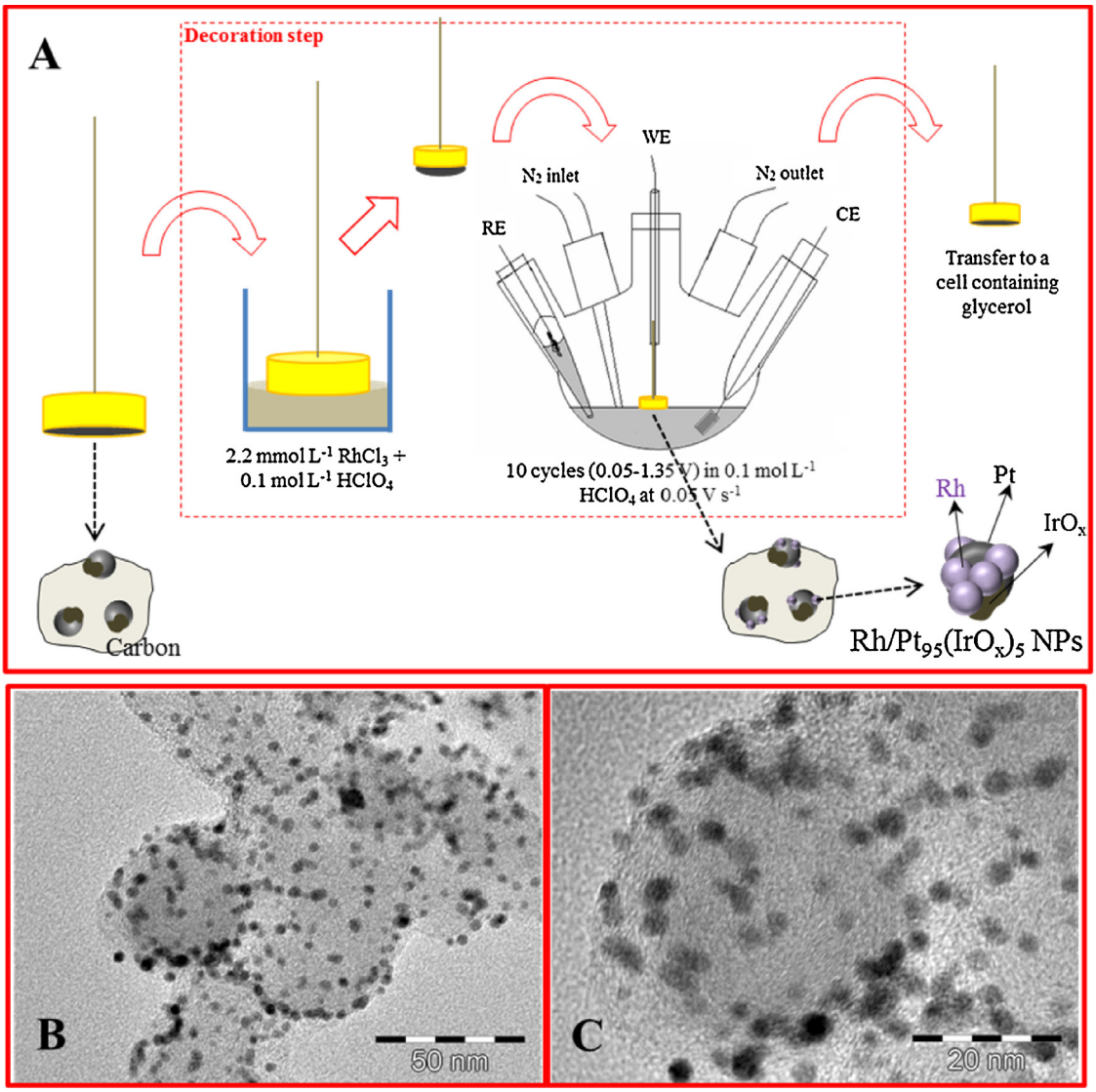

Fig. 6. A. Scheme of the electrochemical decoration of $Pt_{95}(IrO_x)_5$/C with Rh; The red dashed rectangle corresponds to one decoration step. The physical model of NPs is merely illustrative. B–C. Micrographs of Rh/$Pt_{95}(IrO_x)_5$/C manufactured following two decoration steps.(For interpretation of the references to colour in this figure legend, the reader is referred to the web version of this article.)

The influence of Rh coverage on the GEOR was analyzed comparing the Rh/$Pt_{95}(IrO_x)$/C, which performed the best electroactivity (two decoration steps) with $Pt_{95}(IrO_x)$/C and Pt/C, as shows Fig. 8. The presence of Rh clearly anticipates the electrooxidation of glycerol. The onset potential taken from the first derivative of the voltammogram (dj/dE curve, not showed) is 0.47 V for Rh/$Pt_{95}(IrO_x)$/C, and ~0.65 V for Pt/C. Therefore, the pI onset potential shifts 150 mV towards lower potentials. Moreover, the decoration with Rh recovers the electrocatalytic activity previously lost due to the presence of IrO_x in terms of current density.

Chronoamperometric experiments were also performed to evaluate the time-dependent activity of the Rh-decorated catalysts. The optimized Rh/$Pt_{95}(IrO_x)$/C catalyst showed a sensible increment of the pseudo stationary current, reaching 14.6 $\mu A\,cm^{-2}$ after 2100 s at 0.6 V (see Fig. S7). The reproducible current-time profile experiences two apexes. The current decays during 10 s, afterwards the curve reaches a first maximum at 95 s followed by a decrease up to ~400 s. Next, the current returns to increase, reaching a new top at 930 s, followed by a monotonously decrease until 2100 s. The specific activities of Rh/$Pt_{95}(IrO_x)_5$/C, $Pt_{95}(IrO_x)_5$/C and Pt/C are 7.72, 6.29 and 4.56 mA mg–Pt^{-1}, respectively, which shows that Rh-decorated Pt NPs containing IrO_x enhances the electroactivity towards glycerol electrooxidation.

Finally, we evaluated the electrochemical stability of the Rh-decorated $Pt_{95}(IrO_x)$/C NPs.

3.5. The electrochemical stability of Rh/$Pt_{95}(IrO_x)_5$/C catalysts

The stability of a catalyst is a critical requirement to achieve durability for commercializing fuel cells. Once a material with a good efficiency is found, it is imperative to determine its electrochemical stability. For instance, it is known that the electric field applied to the NPs in fuel cells causes physical–chemical changes, which lead to relevant changes in the electrochemical response, generally resulting in loss of efficiency [21,53].

The effects caused by the operation of a fuel cell can be mimicked by a degradation test protocol in a half-cell, which consists in submitting an electrode to successive cyclic voltammetries [53,54]. On this sense, the electrochemical stability of the catalysts was studied by applying 10,000 cycles between 0.05 and 1.35 V at 0.1 V s^{-1}, which is an aggressive condition and might provoke more intense degradation than that experienced by fuel cells [54].

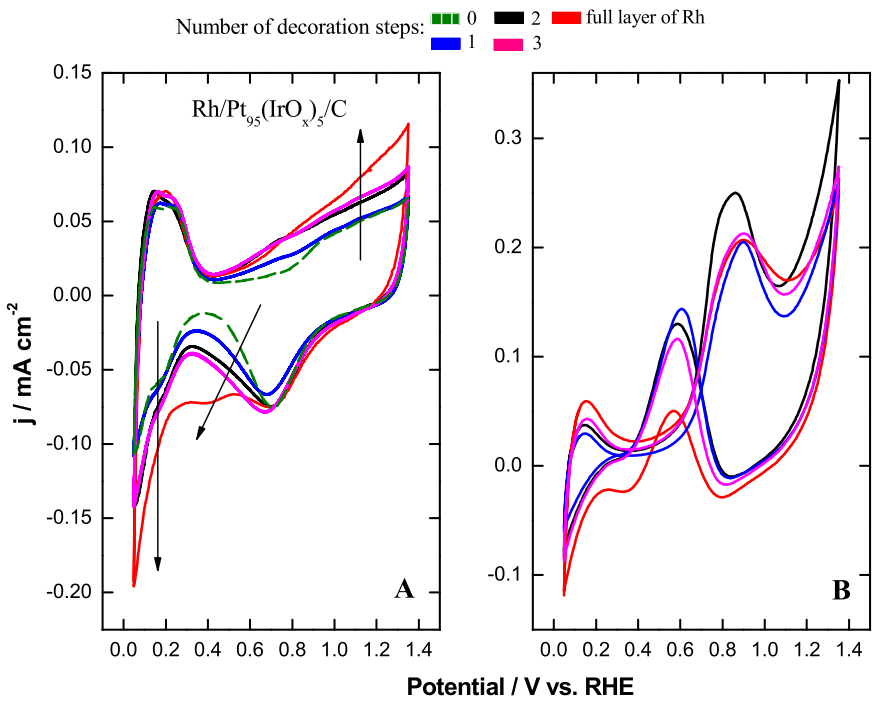

Fig. 7. Stable voltammetric profile for $Pt_{95}(IrO_x)_5/C$ nanoparticles decorated with increasing amounts of Rh in 2.2 mmol L^{-1} $RhCl_3$ + 0.1 mol L^{-1} $HClO_4$ solution in the absence (A) and presence (B) of 0.2 mol L^{-1} glycerol. Increasing amounts of Rh are indicated by an arrow in (A). The colors of the curves correspond to the same electrode in both graphs. Sweep rate = 0.05 V s^{-1}.(For interpretation of the references to colour in the text, the reader is referred to the web version of this article.)

Therefore, in Fig. 9 we compared the electrochemical stability of $Rh/Pt_{95}(IrO_x)/C$ (micrographs, profile and activity showed in Figs. 6B–C, Fig. 7A-black curve and Fig. 8, respectively) with non-decorated $Pt_{95}(IrO_x)/C$ and Pt/C, all presented as an average of 3 independent experiments. The representative voltammograms correlated to the degradation test are presented in Fig. S9 and show the global decrease of currents (hydrogen UPD and formation/reduction of oxides regions are affected) due to the loss of area.

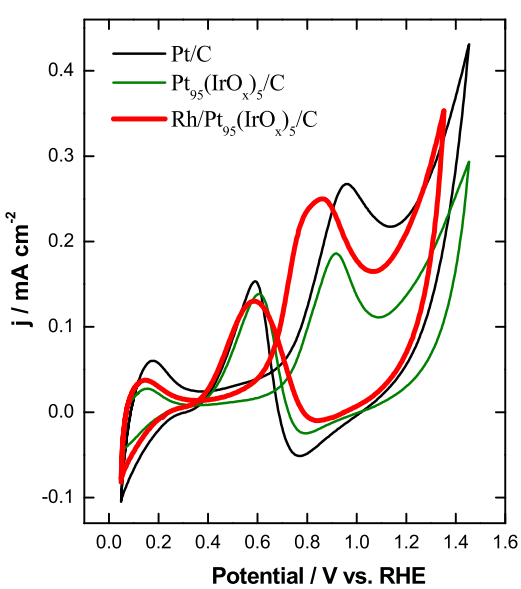

Fig. 8. Stable voltammetric profile for $Rh/Pt_{95}(IrO_x)_5/C$ (red curve), $Pt_{95}(IrO_x)_5/C$ (green curve) and Pt/C (black curve) nanoparticles in 0.1 mol L^{-1} $HClO_4$ + 0.2 mol L^{-1} glycerol at 0.05 V s^{-1}. (For interpretation of the references to colour in this figure legend, the reader is referred to the web version of this article.)

The normalized ECSA ($ECSA/ECSA_{initial}$) decreases continuously through the progress of cycles for all catalysts. The initial degradation is probably related to the dissolution of the smallest NPs and to the agglomeration of those NPs that are close to each other [21,31,55], while the detachment of NPs (mainly caused by the degradation of the support) dominates the behavior observed for long-term applied potentials [21,53].

The ECSA decay follows the order $Rh/Pt_{95}(IrO_x)_5/C < Pt_{95}(IrO_x)_5/C < Pt/C$. More specifically, the catalyst containing IrO_x presents an increase of electrochemical stability during the degradation test and the Rh-decorated nanocatalysts show a remarkable performance compared to Pt/C. After 5000 cycles, at the point where the support degradation starts to dominate the loss of area [21,53], Pt/C showed 76% of

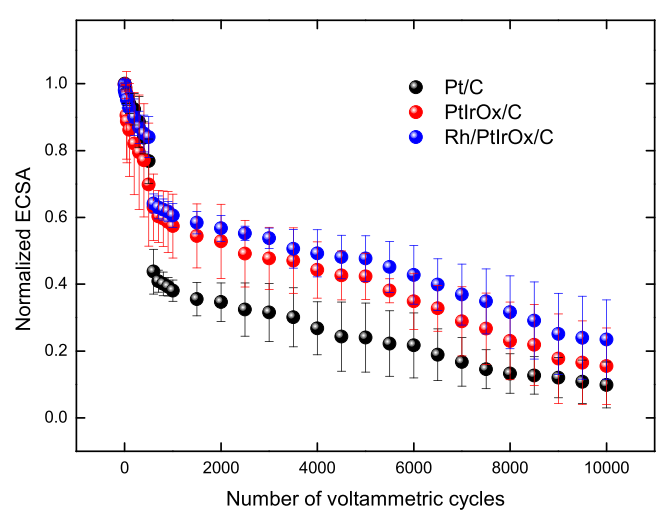

Fig. 9. Electrochemically surface area normalized by the initial surface area in function of the potential cycling. Surface areas obtained from voltammograms performed in 0.1 mol L^{-1} $HClO_4$ at 0.1 V s^{-1} for Pt/C, $Pt_{95}(IrO_x)_5/C$ and $Rh/Pt_{95}(IrO_x)_5/C$.

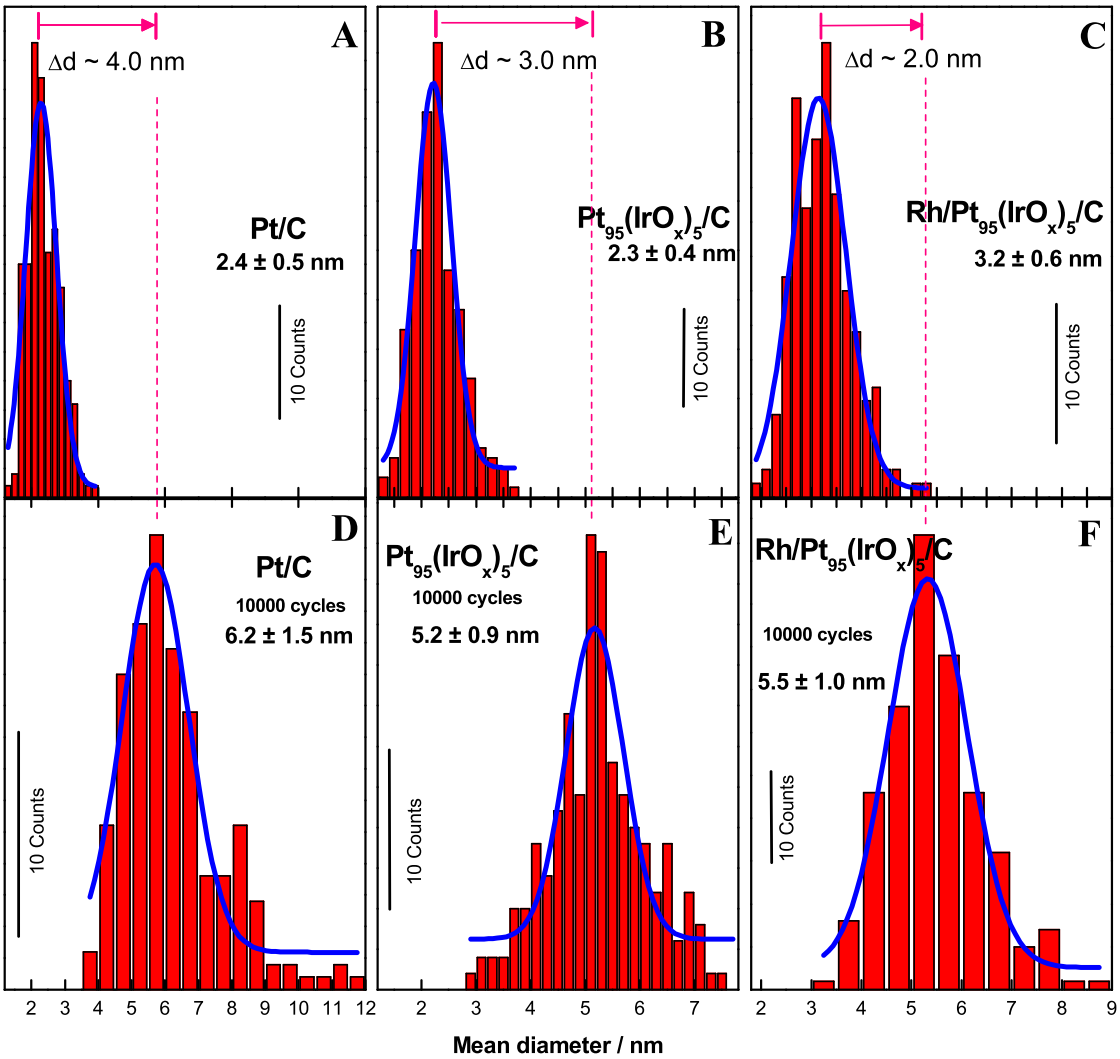

Fig. 10. Histograms, Gaussian of distribution and mean diameter for the conditioned (A–C) and degraded (D–F) Pt/C, $Pt_{95}(IrO_x)_5$/C and Rh/ $Pt_{95}(IrO_x)_5$/C nanoparticles. Mean diameter calculated by counting 200 nanoparticles. The magenta arrows indicate the increase of the mean size of the nanoparticles after 10,000 cyclic voltammograms in acid media.(For interpretation of the references to colour in this figure legend, the reader is referred to the web version of this article.)

loss, while $Pt_{95}(IrO_x)_5$/C and Rh/$Pt_{95}(IrO_x)_5$/C lose 60% and 55%, respectively. At the end of the degradation test, Rh/$Pt_{95}(IrO_x)_5$/C showed the highest normalized ECSA. The main factor for the low long-term stability is the low resilience of the support [53,56]. Considering the high stability in short-terms for those electrodes containing IrO_x/C, the use of different supports as graphene or multi-walled carbon nanotubes is expected to improve the overall electrochemical stability [53]. The most important step during the degradation protocol seems to lie at around 500 cycles, when the ECSA curve suddenly drops. Our results do not allow to rationalize this step and more studies regarding a physical model of the NPs are needed. However, there are strong empirical evidences that Rh-decorated platinum NPs containing iridium oxides remarkably improve the electrochemical stability of the catalyst which is an extremely important result from the technological point of view.

The electrochemical stability of an anode in a fuel cell is directly related to the ability of avoiding NPs agglomeration. As shown in Fig. 9, the decrease of ECSA for the three catalysts evaluated indicates agglomeration of the NPs in all cases. After the degradation test, we removed the NPs from the Au disk to evaluate their morphology by TEM and HRTEM. Fig. S10 shows micrographs of Pt/C, $Pt_{95}(IrO_x)_5$/C and Rh/$Pt_{95}(IrO_x)_5$/C NPs after 10,000 cyclic voltammetries. The agglomeration of NPs leads to an obvious increase in their sizes and a consequent decrease of surface area. The micrographs of Fig. S10 show massive aggregates of Pt NPs compared to the IrO_x containing nanomaterials. We also have found some polygonal particles after the degradation test of Rh/$Pt_{95}(IrO_x)_5$/C NPs, which is in line with a previous work concerning the stability of Pd/C NPs [31].

Based on micrographs, as those showed in Fig. S10, we compared the size distribution of Rh/$Pt_{95}(IrO_x)_5$/C, $Pt_{95}(IrO_x)_5$/C and Pt/C nanomaterials before and after the degradation test protocol, as shows Fig. 10. After the initial surface conditioning Pt/C and $Pt_{95}(IrO_x)_5$/C NPs have approximately the same size (Fig. 10A and B). The enlargement of the mean diameter (Δd in Fig. 10) is less intense for $Pt_{95}(IrO_x)_5$/C NPs than for Pt/C, corresponding to 3 and 4 nm, respectively, which suggests that IrO_x enhances the stability of Pt NPs. The smallest increasing of mean diameter was found for Rh/$Pt_{95}(IrO_x)_5$/C (Fig. 10C and F). The conditioned Rh-decorated NPs have initial mean diameter of about 3.2 nm and increase to approximately 5.5 nm, corresponding to Δd ~2.0 nm. Therefore, the presence of rhodium in the catalyst architecture assists the iridium oxides on promoting high stability for platinum NPs.

In summary, we have demonstrated how to easily design Rh-decorated $PtIrO_x$/C electrodes towards more active and stable catalysts to be used as anodes in direct glycerol fuel cells. The

main role of the additional metals can be rationalized as: (i) IrO_x enhances the electrochemical stability and activity in terms of current density, while (ii) Rh shifts the onset potential of glycerol electrooxidation towards more negative potentials. Therefore, the electrochemical decoration of Pt catalysts containing IrO_x with Rh seems to be an interesting alternative of aggregating multiple electrocatalytic characteristics as: (i) remarkably well dispersed NPs; (ii) high stability; (iii) activity in terms of current density and specific activity; and (iv) anticipation of glycerol electrooxidation in terms of potential. A similar strategy could be followed for manufacturing Rh-decorated Pt-MO_x NPs (where, MO_x can be SnO_2, RuO_2, etc.) with lower cost and immobilized on different carbon supports, for achieve long-term stability.

4. Conclusions

- The polyol reduction method assisted by microwaves is a fast and handleable way to synthesize remarkably well dispersed carbon-supported $PtIrO_x$ nanoparticles;
- The electrooxidation of glycerol on $PtIrO_x$/C is strongly influenced by the composition of the surface. Among the catalysts studied, $Pt_{95}(IrO_x)_5$/C NPs present the highest current densities for glycerol oxidation;
- Throughout a simple electrochemical protocol it is possible to decorate these nanoparticles *a posteriori* in a controllable way. Here the $Pt_{95}(IrO_x)_5$/C catalyst was decorated with Rhodium;
- The decoration step increases the mean average size of the nanoparticles, but sensibly enhances the electrochemical stability of the catalysts during the 5000 potential cycles;
- IrO_x enhances the electrochemical stability, whereas the decorated Rh/$Pt_{95}(IrO_x)_5$/C catalyst shows the best catalytic response towards the electrooxidation of glycerol;
- Our findings illustrate that nanoscaled designed catalysts can be obtained throughout a relative simple protocol and opens up the possibility of testing multi metallic combinations in a controlled manner.

Acknowledgements

The authors acknowledge financial assistance from CAPES, CNPq (Grants # 454516/2014-2 and 479007/2013-6) and FUNDECT (Grants # 23/200.065/2008, # 23/200.625/2012 and # 23/200.583/2012). G.A. Camara acknowledges CNPq (grants # 405695/2013-6 and # 305494/2012-0) and FUNDECT (grant # 23/200.583/2012) for the financial support.

Appendix A. Supplementary data

Supplementary data associated with this article can be found, in the online version, at http://dx.doi.org/10.1016/j.apcatb.2015.08.021

References

[1] W. Zhou, Z. Zhou, S. Song, W. Li, G. Sun, P. Tsiakaras, Q. Xin, Appl. Catal. B 46 (2003) 273–285.
[2] Y. Holade, C. Morais, K. Servat, T.W. Napporn, K.B. Kokoh, ACS Catal. 3 (2013) 2403–2411.
[3] M.J. Giz, G.A. Camara, J. Electroanal. Chem. 625 (2009) 117–122.
[4] G.A. Camara, T. Iwasita, J. Electroanal. Chem. 578 (2005) 315–321.
[5] P.S. Fernández, M.E. Martins, G.A. Camara, Electrochim. Acta 66 (2012) 180–187.
[6] A. Zalineeva, A. Serov, M. Padilla, U. Martinez, K. Artyushkova, S. Baranton, C. Coutanceau, P.B. Atanassov, J. Am. Chem. Soc. 136 (2014) 3937–3945.
[7] C.A. Martins, M.J. Giz, G.A. Camara, Electrochim. Acta 56 (2011) 4549–4553.
[8] P.S. Fernández, M.E. Martins, C.A. Martins, G.A. Camara, Electrochem. Commun. 15 (2012) 14–17.
[9] C.A. Martins, P.S. Fernández, H.E. Troiani, M.E. Martins, G.A. Camara, J. Electroanal. Chem. 717–718 (2014) 231–236.
[10] J.F. Gomes, G. Tremiliosi-Filho, Electrocatalysis 2 (2011) 96–105.
[11] P.S. Fernández, C.A. Martins, M.E. Martins, G.A. Camara, Electrochim. Acta 112 (2013) 686–691.
[12] Y. Kwon, K.J.P. Schouten, M.T.M. Koper, ChemCatChem 3 (2011) 1176–1185.
[13] Y. Kwon, Y. Birdja, I. Spanos, P. Rodriguez, M.T.M. Koper, ACS Catal. 2 (2012) 759–764.
[14] M. Li, W.P. Zhou, N.S. Marinkovic, K. Sasaki, R.R. Adzic, Electrochim. Acta 104 (2013) 454–461.
[15] N. Erini, R. Loukrakpam, V. Petkov, E.A. Baranova, R. Yang, D. Teschner, Y. Huang, S.R. Brankovic, P. Strasser, ACS Catal. 4 (2014) 1859–1867.
[16] L.C. Silva Jr., G. Maia, R.R. Passos, E.A. de Souza, G.A. Camara, M.J. Giz, Electrochim Acta 112 (2013) 612–619.
[17] R.S. Ferreira Jr., M.J. Giz, G.A. Camara, J. Electroanal. Chem. 697 (2013) 15–20.
[18] A. Kowal, M. Li, M. Shao, K. Sasaki, M.B. Vukmirovic, J. Zhang, N.S. Marinkovic, P. Liu, A.I. Frenkel, R.R. Adzic, Nat. Mater. 8 (2009) 325–330.
[19] M. Li, A. Kowal, K. Sasaki, N. Marinkovic, D. Su, E. Korach, P. Liu, R.R. Adzic, Electrochim. Acta 55 (2010) 4331–4338.
[20] R.F.B. De Souza, L.S. Parreira, D.C. Rascio, J.C.M. Silva, E. Teixeira-Neto, M.L. Calegaro, E.V. Spinace, A.O. Neto, M.C. Santos, J. Power Sources 195 (2010) 1589–1593.
[21] J.C. Meier, C. Galeano, I. Katsounaros, J. Witte, H.J. Bongard, A.A. Topalov, C. Baldizzone, S. Mezzavilla, F. Schüth, K.J.J. Mayrhofer, Beilstein J. Nanotechnol. 5 (2014) 44–67.
[22] E. Antolini, ACS Catal. 4 (2014) 1426–1440.
[23] M. Wesselmark, B. Wickman, C. Lagergren, G. Lindbergh, Electrochim. Acta 111 (2013) 152–159.
[24] T. Reier, M. Oezaslan, P. Strasser, ACS Catal. 2 (2012) 1765–1772.
[25] J. Ribeiro, D.M. dos Anjos, K.B. Kokoh, C. Coutanceau, J.-M. Léger, P. Olivi, A.R. de Andrade, G. Tremiliosi-Filho, Electrochim. Acta 52 (2007) 6997–7006.
[26] N. Ehab, E. Sawy, H.M. Molero, V.I. Birss, Electrochim. Acta 117 (2014) 202–210.
[27] V. Armendariz, C.A. Martins, H.E. Troiani, L.C. Oliveira, J.M. Stropa, G.A. Camara, M.E. Martins, P.S. Fernández, Electrocatalysis 5 (2014) 279–287.
[28] J. Schnaidt, M. Heinen, D. Denot, Z. Jusys, J. Behm, J. Electroanal. Chem. 661 (2011) 250–264.
[29] C. Coutanceau, P. Urchaga, S. Brimaud, S. Baranton, Electrocatalysis 3 (2012) 75–87.
[30] P.S. Fernández, D.S. Ferreira, C.A. Martins, H.E. Troiani, G.A. Câmara, M.E. Martins, Electrochim. Acta 98 (2013) 25–31.
[31] C.A. Martins, P.S. Fernández, H.E. Troiani, M.E. Martins, A. Arenillas, G.A. Camara, Electrocatalysis 5 (2014) 204–212.
[32] D.A. Shirley, Phys. Rev. B 5 (1972) 4709–4714.
[33] J.H. Scofield, J. Electron Spectrosc. 8 (1976) 129–137.
[34] J. Cheng, H. Zhang, H. Ma, H. Zhong, Y. Zou, Electrochim. Acta 55 (2010) 1855–1861.
[35] I. Jang, I. Hwang, Y. Tak, Electrochim. Acta 90 (2013) 148–156.
[36] S. Siracusano, V. Baglio, A. Stassi, R. Ornelas, V. Antonucci, A.S. Arico, Int. J. Hydrogen Energ. 36 (2011) 7822–7831.
[37] L. Wang, Q. Han, S. Hu, D. Li, P. Zhang, S. Chen, J. Xu, B. Liu, Appl. Catal. B: Environ. 164 (2015) 128–134.
[38] T.L. Lomocso, E.A. Baranova, Electrochim. Acta 56 (2011) 8551–8558.
[39] H.E. Swanson, E. Tatge, Nat. Bur. Std. U.S, Circ. 539 1953 69–70.
[40] S.G. da Silva, M.H.M.T. Assumpção, R.F.B. de Souza, G.S. Buzzo, E.V. Spinacé, A.O. Neto, J.C.M. Silva, Electrocatalysis 4 (2014) 438–444.
[41] T. Ungar, J. Gubicza, G. Ribarik, C. Pantea, T.W. Zerda, Carbon 40 (2002) 929–937.
[42] B. Podlovchenko, G. Shterev, R. Semkova, E. Kolyadko, Electrochim. Acta 35 (1990) 191–197.
[43] H. Elzanowska, E. Miasek, V.I. Birss, Electrochim. Acta 53 (2008) 2706–2715.
[44] Th. Pauporté, F. Andolfatto, R. Durand, Electrochim. Acta 45 (1999) 431–439.
[45] B.E. Conway, J. Mozota, Electrochim. Acta 28 (1983) 9–16.
[46] G.G. Láng, G. Horányi, J. Electroanal. Chem. 552 (2003) 197–211.
[47] P. Kaghazchi, F.C. Simeone, K.A. Soliman, L.A. Kibler, T. Jacob, Faraday Discuss. 140 (2008) 69–80.
[48] J.F. Gomes, C.A. Martins, M.J. Giz, G. Tremiliosi-Filho, G.A. Camara, J. Catal. 301 (2013) 154–161.
[49] J.F. Gomes, F.B.C. de Paula, L.H.S. Gasparotto, G. Tremiliosi-Filho, Electrochim. Acta 76 (2012) 88–93.
[50] P.S. Fernández, C.A. Martins, C.A. Angelucci, J.F. Gomes, G.A. Camara, M.E. Martins, G. Tremiliosi-Filho, ChemElectroChem 2 (2014) 263–268.
[51] W. Chen, S. Chen, J. Mater. Chem. 21 (2011) 9169–9178.
[52] F.J. Vidal-Iglesias, A. López-Cudero, J. Solla-Gullón, J.M. Feliu, Angew. Chem. 125 (2013) 998–1001.
[53] C.A. Martins, P.S. Fernández, F. de Lima, H.E. Troiani, M.E. Martins, A. Arenillas, G. Maia, G.A. Camara, Nano Energ. 9 (2014) 142–151.
[54] Y.C. Park, K. Kakinuma, M. Uchida, H. Uchida, M. Watanabe, Electrochim. Acta 123 (2014) 84–92.
[55] Y. Shao-Horn, W.C. Sheng, S. Chen, P.J. Ferreira, E.F. Holby, D. Morgan, Top. Catal. 46 (2007) 285–305.
[56] M. Mathias, R. Makharia, H. Gasteiger, J. Conley, T. Fuller, C. Gittleman, S. Kocha, D. Miller, C. Mittesteadt, T. Xie, S. Yan, P. Yu, Electrochem. Soc. Interface 14 (2005) 24–35.